Open Access Article. Published on 15 October 2025. Downloaded on 5/10/2026 3:55:54 AM.
This article is licensed under a Creative Commons Attribution-NonCommercial 3.0 Unported Licence.

RSC Advances

PAPER

View Article Online
View Journal | View Issue

Check for updates

Cite this: *RSC Adv.*, 2025, **15**, 38659

Electronic, optical, magnetocaloric, and thermoelectric properties of $La_{0.5}Sm_{0.2}Sr_{0.3}MnO_3$: a first-principles DFT-MFT investigation

Ala Eddin Mabrouki, *[ab] Khouloud Abdouli,[c] Afrah Bardaoui,[d] Olfa Messaoudi,[e] Latifah Alfhaid[e] and Amjad S. Aljaloud[e]

Received 1st September 2025
Accepted 5th October 2025

DOI: 10.1039/d5ra06540b

rsc.li/rsc-advances

Density functional theory (DFT + U) and mean-field theory (MFT) calculations were carried out on $La_{0.5}Sm_{0.2}Sr_{0.3}MnO_3$ to investigate its electronic, magnetic, and optical properties using the Wien2k package. The total density of states and band structure indicate a semi-metallic ferromagnetic nature. Magnetic properties analyzed with MFT reproduced magnetization isotherms and magnetic entropy ($-\Delta S$) curves, consistent with ferromagnetic behavior. The good agreement between experiment and simulation highlights the reliability of the employed model in predicting the magnetocaloric properties of $La_{0.5}Sm_{0.2}Sr_{0.3}MnO_3$. Optical parameters, including dielectric constants $\varepsilon_1(\omega)$ and $\varepsilon_2(\omega)$, absorption coefficient $\alpha(\omega)$, and optical conductivity, were studied over 0–14 eV. The Seebeck coefficient (S) decreases with temperature, and its positive sign confirms hole conduction. The figure of merit attains a maximum $ZT = 1.22$ at 200 K.

1 Introduction

Perovskite manganites have attracted extensive attention due to their fascinating multifunctional properties and wide range of technological applications.[1–5] Among these, $LaMnO_3$ is particularly important because of its ferroelectric behavior, high dielectric constant, spontaneous polarization, and nonlinear optical properties.[6–8] This material is used in many different devices, including multilayer ceramic capacitors,[9,10] bolometers,[11] and infrared detectors. Furthermore, La-based manganites stand out within the perovskite family due to their rich interplay of structural, electronic, and magnetic degrees of freedom, which can be finely tuned by chemical substitution or external stimuli. Doping in $LaMnO_3$ plays a crucial role in tailoring its physical behavior. The parent compound shows antiferromagnetic ordering at low temperature, whereas substitution with divalent cations (*e.g.*, Sr^{2+}, Ca^{2+}, or Ba^{2+}) induces mixed-valence states of Mn, promoting double-exchange interactions that can drive the system into ferromagnetic and metallic states. Loshkareva *et al.*[12] investigated the effects of light n- and p-type doping on the optical spectra of $LaMnO_3$ and reported substantial modifications in electronic structure, including shifts in absorption edges and additional absorption features. Importantly, both doping types led to electronic phase separation, highlighting the complex interplay between charge, orbital, and spin degrees of freedom in this system.

Beyond magnetism and electronic transport, $LaMnO_3$ exhibits promising thermoelectric properties, with a positive Seebeck coefficient indicating predominant p-type behavior.[3,13] Although its dimensionless figure of merit (ZT) is moderate (0.1–0.3), structural engineering and cation substitution have been suggested as effective strategies to enhance thermoelectric efficiency. Simultaneously, the compound displays complex magnetic transitions between antiferromagnetic and ferromagnetic states, making it a candidate for magnetocaloric applications.

Theoretical approaches (*e.g.* density functional theory (DFT) and the Bean–Rodbell) are considered fundamental pillars of materials science. DFT is particularly valuable because it enables accurate prediction of material properties at the atomic scale using quantum mechanics. It provides insight into electronic structure, magnetism, and thermal behavior without relying solely on costly experiments. Moreover, DFT supports the design of advanced materials for applications in semiconductors, batteries, and solar cells, making it an indispensable tool for both research and industrial innovation. In parallel, the mean field theory plays a key role in describing magnetic phase transitions in systems where magnetism is strongly coupled with structural changes. By incorporating the effect of cationic disorder, this model offers a reliable framework for predicting the magnetocaloric effect. Sclauzero *et al.* combined density functional theory (DFT) with dynamical

---

[a] *Faculty of Sciences of Gafsa, Gafsa 2112, Tunisia*

[b] *Laboratory of Applied Physics, Faculty of Sciences of Sfax University of Sfax, B. P. 1171, 3000 Sfax, Tunisia*

[c] *Faculty of Sciences University of Sfax, B. P. 1171, Sfax 3000, Tunisia*

[d] *Laboratory of Nanomaterials and Systems for Renewable Energies (LaNSER), Research and Technology Center of Energy (CRTEn), Techno-Park Borj Cedria, 2050, Tunis, Bp 95, Hammam-Lif, Tunisia*

[e] *Department of Physics, College of Sciences, University of Ha'il, P. O. Box 2440, Ha'il, Saudi Arabia*

© 2025 The Author(s). Published by the Royal Society of Chemistry

Open Access Article. Published on 15 October 2025. Downloaded on 5/10/2026 3:55:54 AM. This article is licensed under a Creative Commons Attribution-NonCommercial 3.0 Unported Licence.

mean-field theory (DMFT) to investigate the impact of epitaxial strain on the structural and electronic properties of $LaVO_3$.[14] More recently, methodological advances in DFT combined with DMFT have enabled a rigorous analysis of electron–electron scattering in correlated materials such as $SrVO_3$, $SrMoO_3$, and $SrRuO_3$.[15] In addition, Arejdal *et al.* employed a hybrid approach that integrates *ab initio* calculations with Monte Carlo simulations (MCS) and the mean-field approximation to study the magnetic properties of the double perovskite Ba_2CoUO_6.[16] While numerous studies have investigated the physical properties of simple perovskites using theoretical approaches such as density functional theory (DFT) and mean-field theory, comparatively fewer works have examined highly mixed systems. Within the $LaMnO_3$ family, mixed perovskite oxides such as $La_{0.5}Sm_{0.2}Sr_{0.3}MnO_3$ are of particular interest. In this compound, the A-site is occupied by a mixture of large cations (La^{3+}, Sm^{3+}, and Sr^{2+}), while Mn occupies the B-site. Partial substitution of La and Sm with Sr modifies the Mn–O–Mn bond geometry, thereby influencing double–exchange interactions and tuning both the transport and magnetic properties. Notably, $La_{0.5}Sm_{0.2}Sr_{0.3}MnO_3$ exhibits colossal magnetoresistance (CMR) and undergoes a second-order paramagnetic-to-ferromagnetic transition with a Curie temperature of about 278 K,[17] making it a promising candidate for spintronic devices and room-temperature sensing applications.

Despite the large number of studies on $LaMnO_3$-based systems, the fundamental electronic, optical, magnetocaloric, and thermoelectric properties of $La_{0.5}Sm_{0.2}Sr_{0.3}MnO_3$ have not yet been systematically explored using first-principles calculations combined with mean-field theory. In this work, we address this gap by employing density functional theory (DFT) together with MFT simulations to provide deeper insight into the intrinsic properties of this compound. Our study not only clarifies the microscopic mechanisms governing its multifunctional behavior but also contributes to the rational design of manganite-based materials for energy conversion and magnetic cooling applications.

2 Experimental details

The glycine-nitrate process (GNP) was used to synthesize the $La_{0.5}Sm_{0.2}Sr_{0.3}MnO_3$ sample. High purity glycine ($C_2H_5NO_2$, 99.9%) and stoichiometric amounts of La $(NO_3)_3\cdot6H_2O$, Sm $(NO_3)_3\cdot6H_2O$, Sr $(NO_3)_2$, Mn $(NO_3)_2\cdot4H_2O$, and Fe $(NO_3)_3\cdot9H_2O$ (each with a purity of least 99.995%) were used in a 1 : 1 molar ratio. All the nitrates were dissolved in distilled water. This solution was heated to 100 °C under magnetic stirring for additional hour. The temperature slowly increased until the solution evaporated and transformed into a clear, viscous gel. The autoignition process began when a crucial temperature of 350 °C was reached. A foam powder was obtained. This powder was ground and calcined to completely eliminate organic residues, yielding the final product.

Phase purity was evaluated using a Phillips powder diffractometer. The analysis was performed with CuKα radiation ($\lambda = 1.5406$ Å) and employed systematic scans that operated at a step size of 0.017° across an angular within the range of $10° \leq 2\theta \leq 100°$. The XRD data were analyzed using the FullProf program based on the Rietveld method.[18]

3 Theoretical considerations

3.1 *Ab initio* calculation details

To explore the electronic properties and to clearly understand the origin of the magnetic and optical properties of the compound $La_{0.5}Sm_{0.2}Sr_{0.3}MnO_3$, a DFT + U calculation was performed using the WIEN2k simulation package.[19] We adopted the structural parameters from our previous study[17] to create a 1 × 1 × 5 supercell containing 10 atoms of La, 6 atoms Sr, 4 atoms of Sm, 20 atoms of Mn, and 60 oxygen atoms. To investigate the electronic properties and to clearly understand the origins of the magnetic and optical properties of this compound, DFT calculations were investigated. To improve the accuracy of the electronic structures of these perovskites while remaining within the DFT framework, it is possible to introduce an in-site Hubbard parameter (GGA + U), adjusted according to the convergence of the total energy. An appropriate value of U_{eff} ($U = U_{\text{eff}} - J$) allows to take into account the Coulomb interactions between the Sm 4f and Mn 3d electrons.[20] The values of U used in this work were 7 eV and 4 eV for the Sm[21] and Mn[20] ions, respectively. To ensure proper convergence for all calculations, the cutoff energy defined as the separation energy between valence and core states was set to −7 Ry (∼−95.24 eV), and the number of *k*-points was set to 2000. The muffin-tin radii (RMT) for La, Sm, Sr, Mn and O atoms were 2.5, 2.4, 2.3, 1.87, and 1.61 a.u., respectively. The plane-wave energy cutoff parameter RMT × KMAX was set to 8.0. The structure was optimized and fully relaxed. The convergence conditions adopted were as follows: the energy variation and the force difference were set to 10^{-3} eV and 10^{-2} eV Å^{-1}, respectively.

The thermoelectric properties were calculated using the Boltzmann transport theory as implemented in the BoltzTrap code.[22] The values of σ and κ are dependent on the relaxation time (τ), which was treated as a constant ($\tau = 10^{-14}$ s) within the BoltzTrap code.

3.2 Mean-field theory (MFT)

The Brillouin equation was used to model the magnetization of a magnetic material:[23,24]

$$M = f\left(\frac{H + H_{\text{exch}}}{T}\right) = M_0 B_j(x) \tag{1}$$

where $M_0 = NJg\mu_B$ represents the saturation magnetization and $B_j(x)$ represents the Brillouin function and expressed as follow:

$$B_J(x) = \frac{2J+1}{2J}\coth\left(\frac{2J+1}{2J}x\right) - \frac{1}{2J}\coth\left(\frac{1}{2J}x\right) \tag{2}$$

where $x = \dfrac{Jg\mu_B}{k_B}\left(\dfrac{H + H_{\text{exch}}}{H}\right)$ and $J = |L \pm S|$ is angular momentum. The orbital and spin momentums (L and S) were linked by Lande factor $g = 1 + \dfrac{J(j+1) + S(S+1) - L(L+1)}{2J(J+1)}$.

In the MFT context, the exchange field H_{exch} is linked to magnetization by this relation:

© 2025 The Author(s). Published by the Royal Society of Chemistry

Open Access Article. Published on 15 October 2025. Downloaded on 5/10/2026 3:55:54 AM.
This article is licensed under a Creative Commons Attribution-NonCommercial 3.0 Unported Licence.

$$\frac{H}{T} = B_J^{-1}(M) - \frac{H_{\text{exch}}}{T} \tag{3}$$

In addition, the magnetic entropy change (ΔS_M) can be simulated by the following form:

$$\Delta S_M(T)_{H_1-H_2} = \int_{M/H_1}^{M/H_2} \left(f^{-1}(M) - \left(\frac{\partial H_{\text{exch}}}{\partial T} \right)_M \right) \mathrm{d}M \tag{4}$$

The order of the magnetic transition is related by the compressibility K, the total momentum J, and spin density N by the following equation:[24]

$$\eta = \frac{5}{2} N k_B K T_0 \beta^2 \frac{[4J(J+1)]^2}{\left[(2J+1)^4 - 1\right]} \tag{5}$$

With k_B is the Boltzmann constant.

The first-order magnetic transition in a material can be defined by $\eta > 1$ value, while $\eta < 1$ denotes a second order transition.[25]

4 Results

4.1 Structural properties

The refined X-ray diffraction (XRD) pattern of the compound $La_{0.5}Sm_{0.2}Sr_{0.3}MnO_3$ (Fig. 1) exhibits sharp and intense peaks indicating the formation of a well-defined crystal structure with no detectable secondary phases. All peaks in the refined profile can be indexed to an orthorhombic unit cell (space group *Pnma*). The crystallographic parameters, including lattice constants (a, b and c), Mn–O bond lengths, Mn–O–Mn bond angles and the reliability factors of the Rietveld refinement, are summarized in Table 1. The goodness of fit was assessed using the R factors and the χ^2 parameter, which indicated excellent agreement between the experimental and calculated patterns.

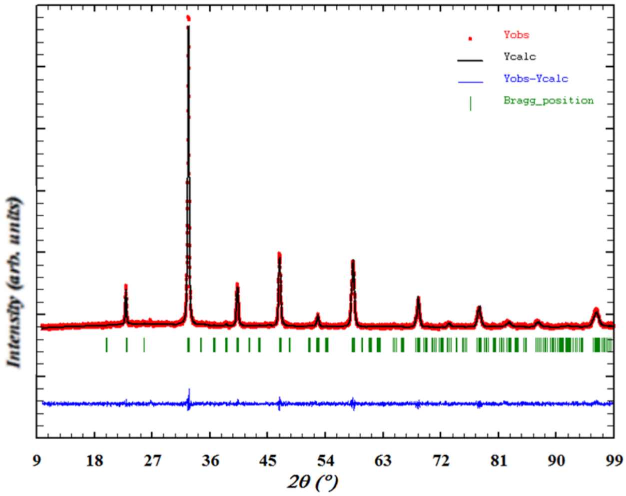

Fig. 1 Rietveld-refined X-ray diffraction patterns of $La_{0.5}Sm_{0.2}Sr_{0.3}MnO_3$ sample: the calculated data is depicted as solid black line, the observed data appeared as red dots, the Bragg reflection positions are represented by green ticks, and the blue line demonstrates the difference between the calculated and observed data.

To understand the principles governing the formation and structural stability of perovskite oxide systems, Goldschmidt introduced the tolerance factor (t_G) as an empirical parameter. This parameter depends on the ionic radii of the A- and B-site cations and the oxygen anion, as well as the degree of octahedral distortion. It is expressed as:

$$t_G = \frac{r_A + r_O}{\sqrt{2}(r_B + r_O)} \tag{6}$$

where r_A represents the average ionic radius of the A-site cations (La, Sm, Sr), r_B is the radius of the B-site cation (Mn), and r_O corresponds to the oxygen anion. For perovskite systems, structural stability is generally achieved within the range $0.75 < t_G < 1$, with maximum symmetry obtained as t_G approaches unity.

Using Shannon's tabulated ionic radii, the tolerance factor of $La_{0.5}Sm_{0.2}Sr_{0.3}MnO_3$ was calculated to be $t_G = 0.92$, supporting that the orthorhombic crystal structure is stable. In addition, the average crystallite size (D) was estimated from the Debye–Scherrer equation:

$$D = \frac{K\lambda}{\beta \cos\theta} \tag{7}$$

where λ is the Cu Kα radiation wavelength, K is the Scherrer constant (0.9), β is the full width at half maximum (FWHM) of the diffraction peak in radians, and θ is the Bragg angle. The calculated crystallite size confirms the nanocrystalline nature of the compound.

Table 1 Structural parameters obtained from Rietveld refinement

Space group		
Cell parameters		*Pnma*
Experimental parameters	a (Å)	5.501
	b (Å)	7.732
	c (Å)	5.469
	V (Å^3)	232.686
Optimized parameters (DFT + U)	a (Å)	5.4762
	b (Å)	7.7573
	c (Å)	5.4867
Agreement factors		
R_p (%)		3.32
R_{WP} (%)		4.21
R_{exp} (%)		3.67
Bragg R-factor(%)		1.83
RF-factor (%)		3.86
χ^2		1.31
Bond lengths		
Mn–O$_1$ (Å)		1.939
Mn–O$_2$ (Å)		2.113
Mn–O$_2$ (Å)		1.823
Bond angles		
Mn–O$_1$–Mn		170.62
Mn–O$_2$–Mn		162.412

Open Access Article. Published on 15 October 2025. Downloaded on 5/10/2026 3:55:54 AM.
This article is licensed under a Creative Commons Attribution-NonCommercial 3.0 Unported Licence.

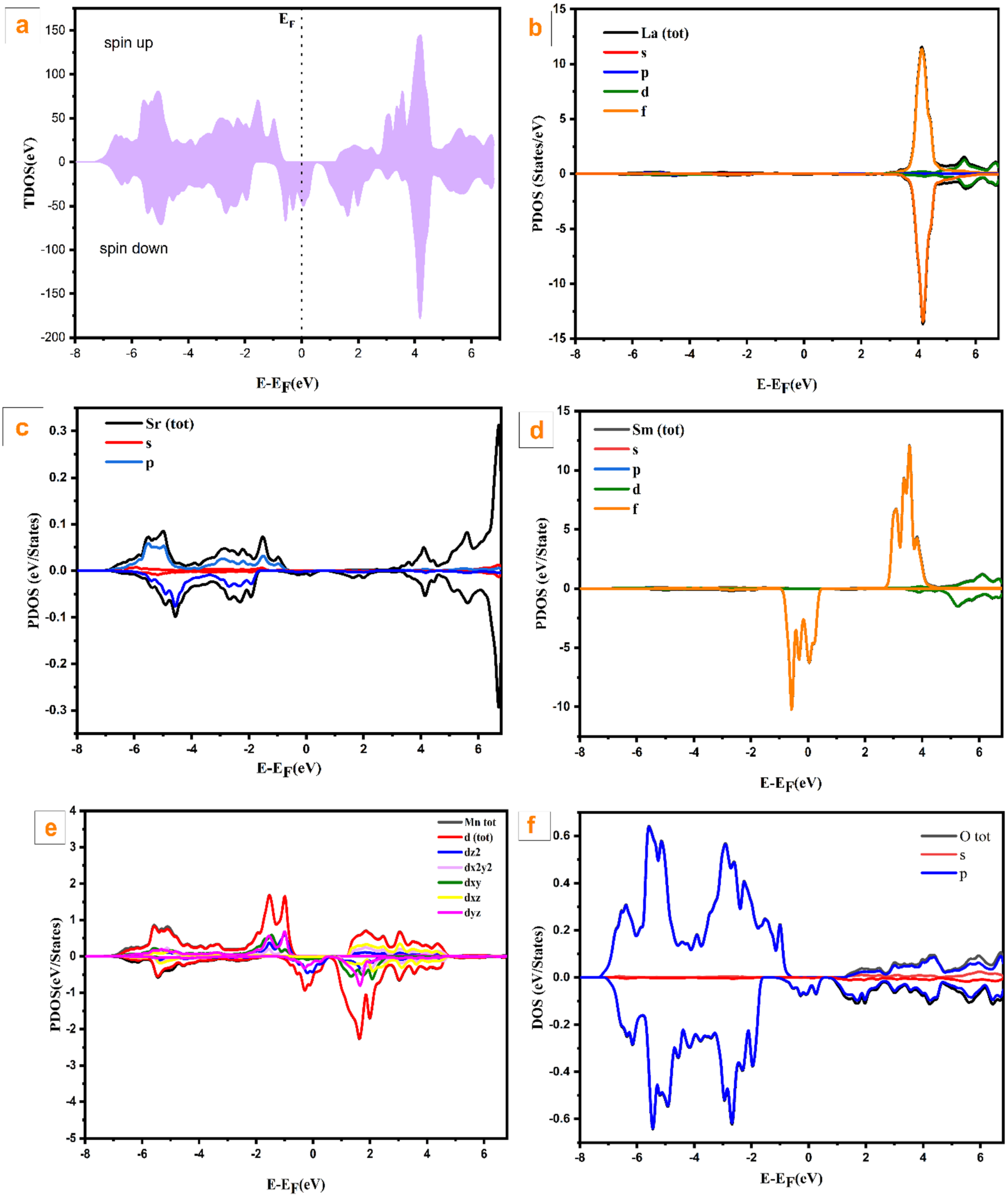

Fig. 2 (a) Total density of states for $La_{0.5}Sm_{0.2}Sr_{0.3}MnO_3$, (b–f) partial density of states of La, Mn 3d, Sm and O.

4.2 Electronic properties

To study the electronic properties of $La_{0.5}Sm_{0.2}Sr_{0.3}MnO_3$ compound, total electronic density of states (TDOS) is shown in Fig. 2a. The density of states (DOS) for the spin-down channel does not drop to zero at the Fermi level (E_F), indicating the presence of electronic states available at E_F. This availability allows for electrical conduction in the spin-down channel, exhibiting metallic behavior. In contrast, the spin-up channel

Open Access Article. Published on 15 October 2025. Downloaded on 5/10/2026 3:55:54 AM.
This article is licensed under a Creative Commons Attribution-NonCommercial 3.0 Unported Licence.

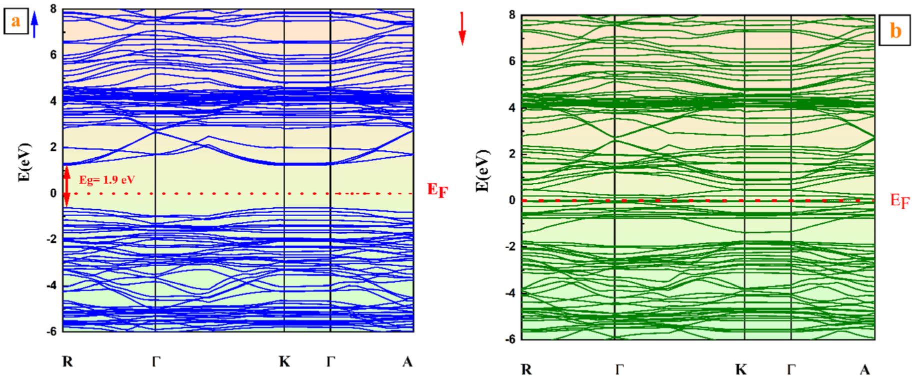

Fig. 3 Band structure (spin up (a) and down (b)) for $La_{0.5}Sm_{0.2}Sr_{0.3}MnO_3$ sample.

shows a band gap, revealing half-metallic behavior of the studied material. Additionally, the TDOS plot shows different distributions for spin-up and spin-down electrons. This asymmetry indicates the ferromagnetic nature of the compound with a calculated total magnetic moment $\sim 3\ \mu_B$.

Fig. 2b–f shows that below −1 eV, the electron energy states are composed of Sr 4p, Mn 3d, and O 2p states. Above ~3 eV, they are mainly contributed by Sr 3d states, while near 4 eV, La and Sm 4f states dominate.

Remarkably, near the Fermi energy (E_F) level, for spin-down, the energy states are primarily composed of Mn 3d, Sm 4f and O 2p. The strong hybridization, at E_F level, between these orbitals indicates enhanced covalent interaction between Mn/Sm, and O ions which contribute to the observed metallic behavior.

The transport mechanism in manganite materials is known to be primarily influenced by electrons situated in the Mn 3d and O 2p orbitals.[20,26] It is well established that the MnO_6 octahedra are deformed due to the presence of a Jahn–Teller type distortion, which also divides the degenerate states of the eg orbital into x^2–y^2 and $3z^2$ states, and the $2t_g$ orbital into $3d_{xy}$, $3d_{xz}$, and $3d_{yz}$. Near the Fermi level, the majority of energy states in the valence band are occupied by Mn: d_{yz}, d_{xz}, d_{xy} and O 2p, while the conducted band is occupied by the Mn $3d_{z^2}$, x^2–y^2, and $3d_{xy}$ orbitals. For the spin up states, the $3d_{z^2}$ orbital is lowered in energy due to compressive stress. Consequently, a band gap develops as valence electrons prefer to occupy the lower energy orbital under these constraints.[27]

Fig. 3 depicts the "spin up and spin down" band structure. The valence states in the spin down cross the Fermi level showing that the free carriers are available to exhibit a metallic character, while in the spin up scenario a semiconducting behavior with a band gap $E_g = 1.9$ eV is observed. Therefore, the overall behavior of the studied compound is half-metallic. By comparing the band structure with the computed DOS, the band gap value can be attributed to the electron density states for Sm 4f, Mn 3d, and O 2p.

4.3 Optical properties

The optical properties of the $La_{0.5}Sm_{0.2}Sr_{0.3}MnO_3$ sample were investigated using the Kramers–Kronig relation. In the field of linear optics, the dielectric functions ε_1 and ε_2 are used to characterize the main optical properties.[28,29] The frequency-dependent dielectric function $\varepsilon(\omega)$, can be expressed as:

$$\varepsilon(\omega) = \varepsilon_1(\omega) + i\varepsilon_2(\omega) \tag{8}$$

where $\varepsilon_1(\omega)$ and $\varepsilon_2(\omega)$ are known to be the real part and imaginary part of the complex dielectric function (Fig. 4).

It is shown that the static real dielectric constant $\varepsilon_1(0)$ exhibits a large value ($\varepsilon_1(0) = 19.27$ eV), which corresponds to the plasmon resonance.[30] As the energy photon increases, $\varepsilon_1(\omega)$ decreases sharply reaching a minimum at 0.32 eV which may be related to the metallic character for the spin down states and the ferroelectric nature of the perovskite.[27] Above $E = 9$ eV, $\varepsilon_1(\omega)$ becomes negative indicating that incident radiation is completely reflected by the surface.[29,31] Fig. 3b shows the variation of $\varepsilon_2(\omega)$ as function of photon energy. Four dielectric peaks E_1, E_2, E_3, and E_4 were observed which agree with the photon energy 1.4 eV, 3.2 eV, 5.8 eV, and 7.6 eV. These peaks are mainly due to electric–dipole transitions between the valence and conduction bands.[32]

According to DOS, the E_1, E_2 dielectric peaks are associated with the electronic transition between the top of the valence band and the bottom of the conduction band, mainly arising from Mn-3d and O-2p orbitals. However, the other peaks originate mainly from the electronic transition between the La-p, Sm 4f, Sr 3p, and O 2s orbitals.

The high absorption in the UV-A range suggest that this material can be used as an absorber in solar cell and other optoelectronic applications.[31]

The optical absorption spectrum shows slightly anisotropic, with the strongest absorption along the y-polarization occurring at 8.5 eV, while the strongest absorption along the *c*-axis occurs at 10 eV.

4.4 Magnetic properties

The magnetic and magnetocaloric properties of the $La_{0.5}Sm_{0.2}Sr_{0.3}MnO_3$ sample were studied in our previous work.[17] The study showed that the present compound exhibits a second order magnetic transition from ferromagnetic state FM to a paramagnetic state PM at $T_C = 278$ K.[17]

Fig. 5 displays the magnetic hysteresis measured at 5 K under a magnetic field range up to 2 T. The graph shows

© 2025 The Author(s). Published by the Royal Society of Chemistry

Open Access Article. Published on 15 October 2025. Downloaded on 5/10/2026 3:55:54 AM.
This article is licensed under a Creative Commons Attribution-NonCommercial 3.0 Unported Licence.

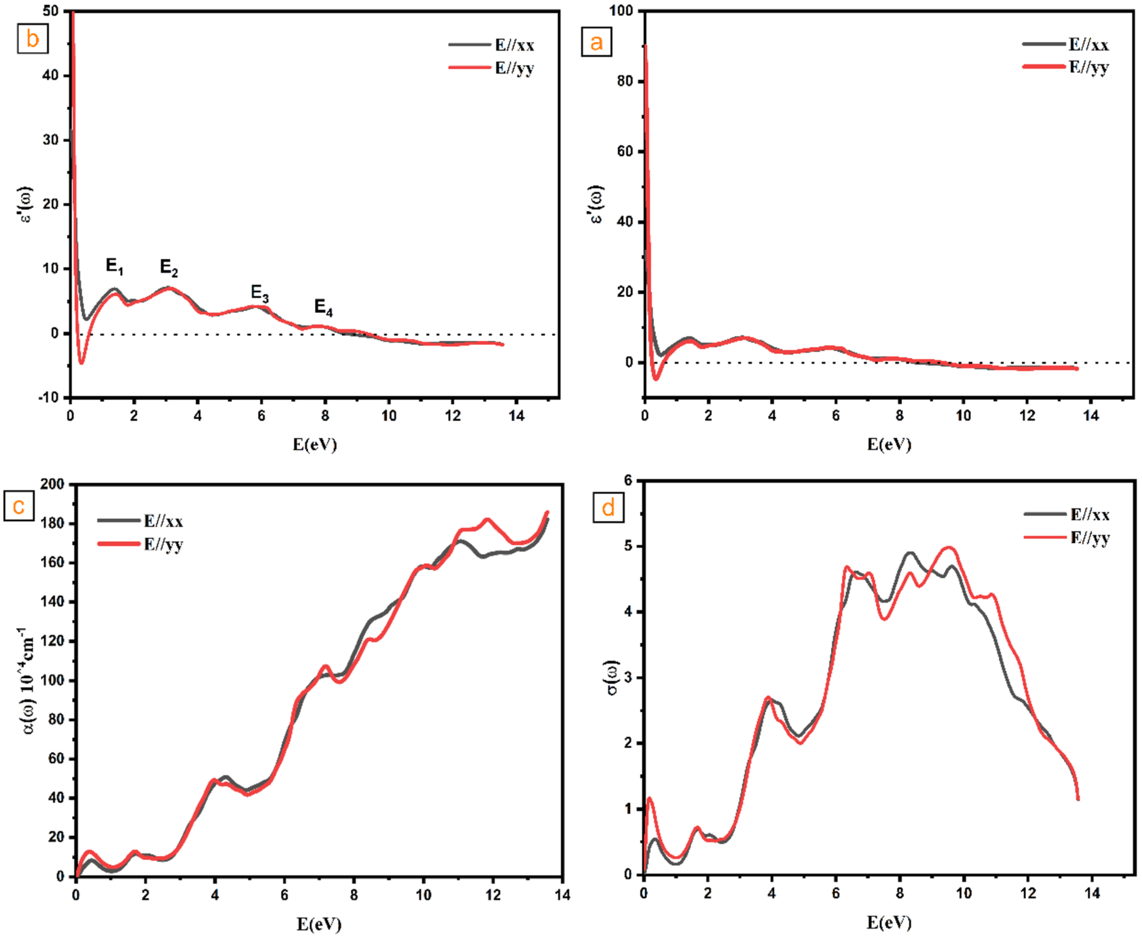

Fig. 4 Optical properties: (a) the real dielectric constants $\varepsilon_1(\omega)$, (b) the imaginary dielectric constants $\varepsilon_2(\omega)$, (c) the absorption coefficient $\alpha(\omega)$, and (d) real part of optical conductivity le long de [100] et [010] directions cristallographiques qui sont représentées respectivement par les directions *xx* et *yy*.

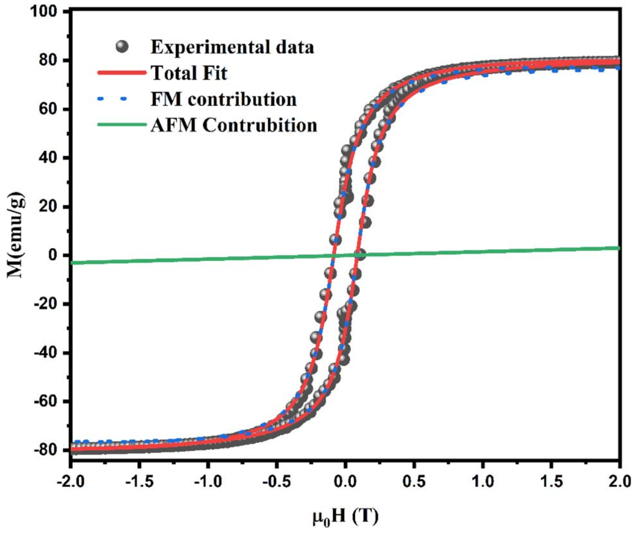

Fig. 5 Magnetic hysteresis measured at 5 K under a magnetic field reaches 2 T.

a typical S-shaped ferromagnetic loop, where magnetization increases rapidly with the applied magnetic field, then saturates at higher fields.

In order to quantify the magnetic parameters saturation magnetization M_s, intrinsic coercivity H_c, and remnant magnetization M_r, the M–H loop was fitted using the following equation:[33]

$$M(H) = 2\frac{M_s}{\pi}\times \text{artan}\left(\frac{H\pm H_c}{H_c}\right)\times \tan\left(\frac{\pi}{2}\times\frac{M_r}{M_s}\right)+\chi H \tag{9}$$

The first term quantifies the FM contributions while the second represents AFM contribution (linear contributions).

The green line (AFM contribution) is nearly zero across the range of the applied magnetic field, suggesting that any antiferromagnetic component is negligible in this material. The saturation magnetization M_s (emu g^{-1}) and the molecular weight MW (g mol^{-1}) are used to calculate the magnetic momentsμ_{fu} (μ_B) according to the following relation.[33,34]

$$\mu_{fu}(\mu_B) = \frac{M_s(\text{emu g}^{-1})\times M_w(\text{g mol}^{-1})}{\mu_B(\text{erg G}^{-1})\times N_A(\text{mol}^{-1})} = \frac{M_s\times M_w}{5585} \tag{10}$$

© 2025 The Author(s). Published by the Royal Society of Chemistry

Open Access Article. Published on 15 October 2025. Downloaded on 5/10/2026 3:55:54 AM. This article is licensed under a Creative Commons Attribution-NonCommercial 3.0 Unported Licence.

Table 2 Magnetic parameters for $La_{0.5}Sm_{0.2}Sr_{0.3}MnO_3$ obtained from the hysteresis loops fitting

	Total	AFM contribution	FM contribution				%	
	μ_{fn} (μ_B) 5 K	χ	H_C (10^{-4} T)	M^S_{FM} (emu g^{-1})	M^R_{FM} (emu g^{-1})	M_R/M_S	FM	AFM
$La_{0.5}Sm_{0.2}Sr_{0.3}MnO_3$	3.5	4.608	875	75	30	0.4	93.75	6.25

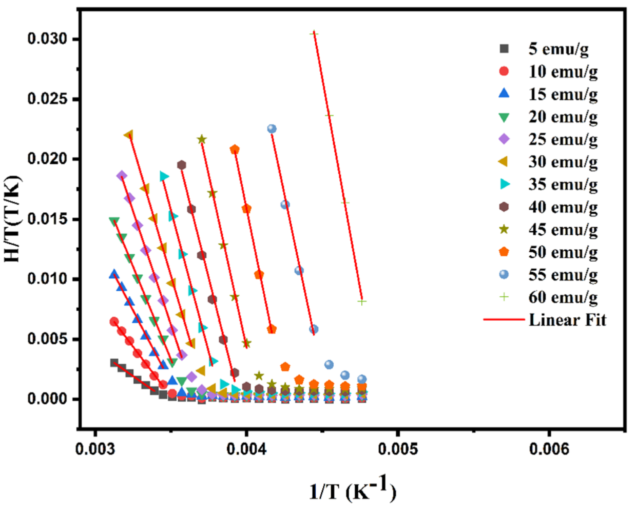

Fig. 6 Variation of H/T *vs.* $1/T$ curves with constant values of magnetization for the $La_{0.5}Sm_{0.2}Sr_{0.3}MnO_3$ sample.

where μ_B is the Bohr magneton and $N_A = 6.022\times 10^{23}$ mol^{-1} is the Avogadro's number. The magnetic parameters extracted from hysteresis (Fig. 5) fitting are summarized in Table 2. It is noticed that the M_r/M_s value is close to 0.5 which presents the theoretical value for randomly oriented single-domain particles.[33]

Amaral *et al.* have developed a good method based on MFT to simulate the magnetization isotherms and $-\Delta S$ curves.[23,35] This approach employs eqn (1) to modify the scaling plot curves of magnetization (M *vs.* $\frac{H+H_{exch}}{T}$) in order to obtain the total momentum J and the saturation magnetization M_s.

To ascertain the H_{exch} values, the fluctuation of $\frac{\mu_0 H}{T}$*vs.*$1/T$ were plotted in Fig. 5, using a constant magnetization value of 5 emu g^{-1}.

Following eqn (4), the H_{exch} values can be determined from the slope of each curve by applying a linear fit in the PM region. The variation of H_{exch} as a function of magnetization M, modified by the following equation, is shown in Fig. 6.

$$H_{exch} = \lambda_1 M + \lambda_3 M^3 \tag{11}$$

It is found that the values of λ_1 and λ_3 are, respectively, 1.5137 and -1.1456×10^{-4} T g^3 emu^{-3}. As opposed to λ_3, the value of λ_1 is significantly high. Consequently, λ_3 is neglected. Thus, the exchange field can be written as follows (Fig. 7).

$$H_{exch} = \lambda_1 M \approx \lambda M \tag{12}$$

M *vs.* $(H + H_{exch})/T$ is plotted in Fig. 8 using a scaling plot. All magnetization isotherms are reduced to a single curve, which has been modified in MATLAB software by adjusting eqn (1) in order to extract the experimental values of M_S, J, and g.[23] Table 3 provides a summary of the acquired values.

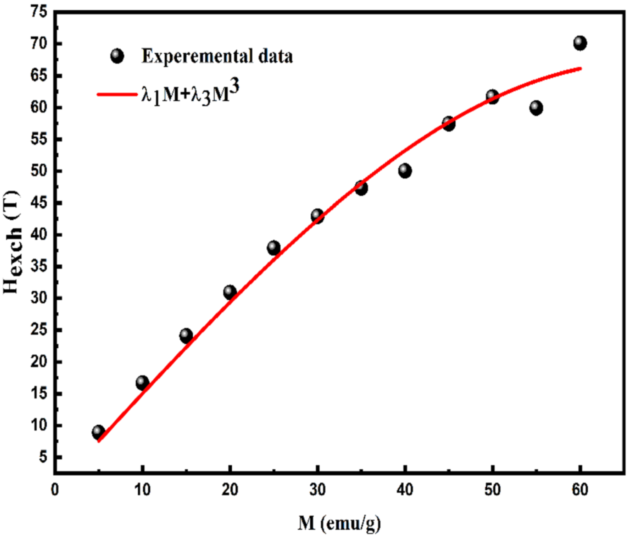

Fig. 7 Exchange field dependence of magnetization for the $La_{0.5}Sm_{0.2}Sr_{0.3}MnO_3$ sample. Red line as the fit by the equation $H_{exch} = \lambda_1 M + \lambda_3 M^3$.

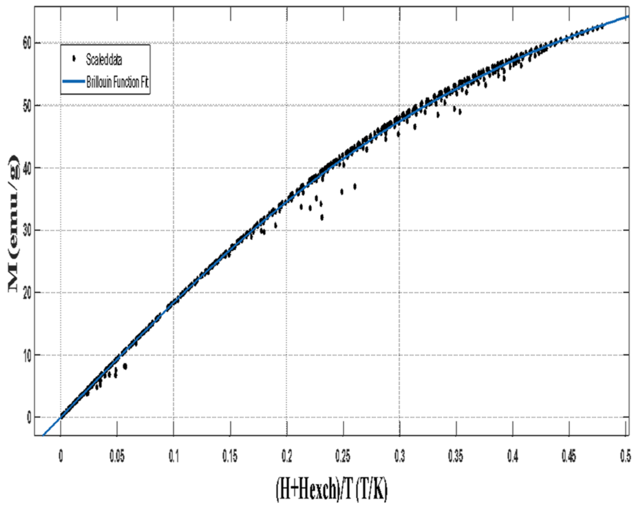

Fig. 8 Scaled data in magnetization *vs.* $(H + H_{exch})/T$ and the Brillouin function fit for the $La_{0.5}Sm_{0.2}Sr_{0.3}MnO_3$ compound.

© 2025 The Author(s). Published by the Royal Society of Chemistry

Open Access Article. Published on 15 October 2025. Downloaded on 5/10/2026 3:55:54 AM.
This article is licensed under a Creative Commons Attribution-NonCommercial 3.0 Unported Licence.

Table 3 The extracted M_S, J, g, λ and, η parameters

Sample	J	g	M_s (emu g^{-1})	T_0 (K)	λ	η
$La_{0.5}Sm_{0.2}Sr_{0.3}MnO_3$	3.2	2.3	79	277.5	1.5137	0.4

The extracted M_S, J, and g values listed in Table 3 are utilized to modulate the M (H, T) and $-\Delta S_M$ curves as illustrated in Fig. 9a and b. These curves are generated using the Magnetocaloric Software Suite (MFSS) running MATLAB.

The good agreement between the experimental and simulated curves proves the pertinence of the employed model for the prediction of $La_{0.5}Sm_{0.2}Sr_{0.3}MnO_3$ magnetocaloric properties.

4.5 Thermoelectric properties

By analyzing the band structures of a material, one can estimate its transport properties using the semi-classical Boltzmann transport theory.[36] The following equations can be implemented to calculate the Seebeck coefficient, electrical conductivity, and thermal conductivity.[3]

$$\sigma_{\alpha\beta}(T,\mu) = \frac{1}{eT\Omega}\int \sigma_{\alpha\beta}(\varepsilon)(\varepsilon-\mu)\left[-\frac{\partial f_\mu(T,\varepsilon)}{\partial\varepsilon}\right]\mathrm{d}\varepsilon \qquad (13)$$

$$k_{\alpha\beta}{}^{0}(T,\mu) = \frac{1}{eT\Omega}\int \sigma_{\alpha\beta}(\varepsilon)(\varepsilon-\mu)^2\left[-\frac{\partial f_\mu(T,\varepsilon)}{\partial\varepsilon}\right]\mathrm{d}\varepsilon \qquad (14)$$

$$S_{\alpha\beta}(T,\mu) = \sigma_{\alpha\beta}(T,\mu)^{-1}\vartheta_{\alpha\beta}(T,\mu) \qquad (15)$$

Fig. 10 illustrates the temperature dependence of the electrical conductivity and thermal conductivity, total Seebeck coefficient, and ZT factor for the $La_{0.5}Sm_{0.2}Sr_{0.3}MnO_3$. As depicted in Fig. 10a, the electrical conductivity for spin-up states exhibits typical behavior of a semiconductor. In this scenario, the conductivity remains constant at low temperatures and experiences an exponential increase at the high-temperature range. This is attributed to the fact that free carrier charges possess higher energy to overcome the potential barrier at elevated temperatures.

The electrical conductivity for spin-down states demonstrates a consistent decline with rising temperature, indicative of metallic behavior. The variations in thermal conductivity as a function of temperature for the spin-up and spin-down states are shown in Fig. 10b.

The total electronic thermal, electrical conductivity, and Seebeck coefficients are given by $= k(\uparrow) + k(\downarrow)$, $\sigma = \sigma(\uparrow) + \sigma(\downarrow)$ and $S = \frac{(S(\uparrow)\sigma(\uparrow) + S(\downarrow)\sigma(\downarrow))}{[\sigma(\uparrow) + \sigma(\downarrow)]}$ where $(\uparrow)$ and $(\downarrow)$ represent the coefficients for spin up and spin down, respectively. Utilizing this model, the total Seebeck coefficient (Fig. 10c) obtained shows a decrease as temperature increases. A positive Seebeck coefficient (S) indicates that holes contribution predominantly governs electric conduction.[37]

Fig. 10d depicts the evolution of the ZT figure of merit as a function of temperature (T). Similar to the Seebeck coefficient, ZT attains the maximum of $ZT = 1.22$, at low temperature 200 K decreasing while maintaining a value above 0.8. The ZT value reaches 1.2 at 300 K, indicating that the material can be considered a viable option for thermoelectric device integration.

Comparing the thermoelectric and magnetocaloric properties of $La_{0.5}Sm_{0.2}Sr_{0.3}MnO_3$ with other similar perovskite-based manganite compounds provides a broader perspective on its performance. For example, Li *et al.* reported a complex structure in $SrTiO_3$, with a TiO_2 secondary phase and a porous morphology. This microstructural design led to an enhanced thermoelectric performance, achieving a ZT value of 0.31 at 1050 K First-principles calculations and high thermoelectric performance of La-Nb doped $SrTiO_3$ ceramics.[38] $Sr_{0.75}Ca_{0.25}Mn_{0.95}V_{0.05}O_{3-\delta}$ material has shown high values of dimensionless figure-of-merit high-temperature thermoelectrical properties of cubic $SrMnO_{3-\delta}$ based manganites.[39] A maximum value of 0.09 for the figure of merit (ZT) is obtained for 0.95 $LaCoO_3$–0.05$La_{0.7}Sr_{0.3}MnO_3$ at 620 K which is significantly higher than the ZT of either of $LaCoO_3$ or $La_{0.7}Sr_{0.3}MnO_3$ at 620 K.[40]

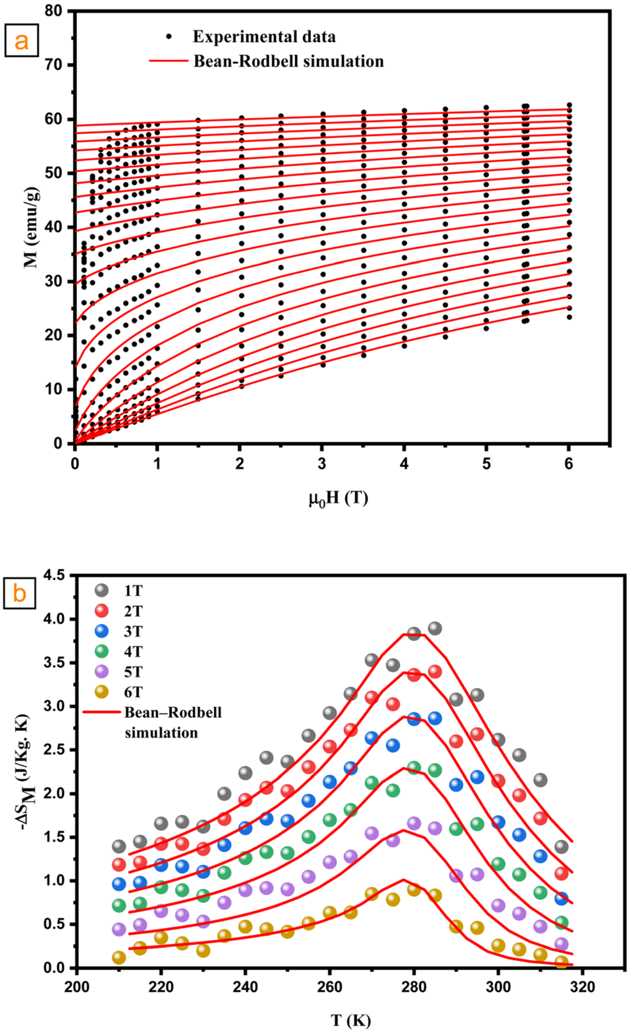

Fig. 9 (a) Experimental (symbols) and simulated (red lines) magnetization M *vs.* μ_0H. (b) Experimental (symbol) and theoretical (red line) magnetic entropy change *versus* temperature under different magnetic fields.

© 2025 The Author(s). Published by the Royal Society of Chemistry

Open Access Article. Published on 15 October 2025. Downloaded on 5/10/2026 3:55:54 AM.
This article is licensed under a Creative Commons Attribution-NonCommercial 3.0 Unported Licence.

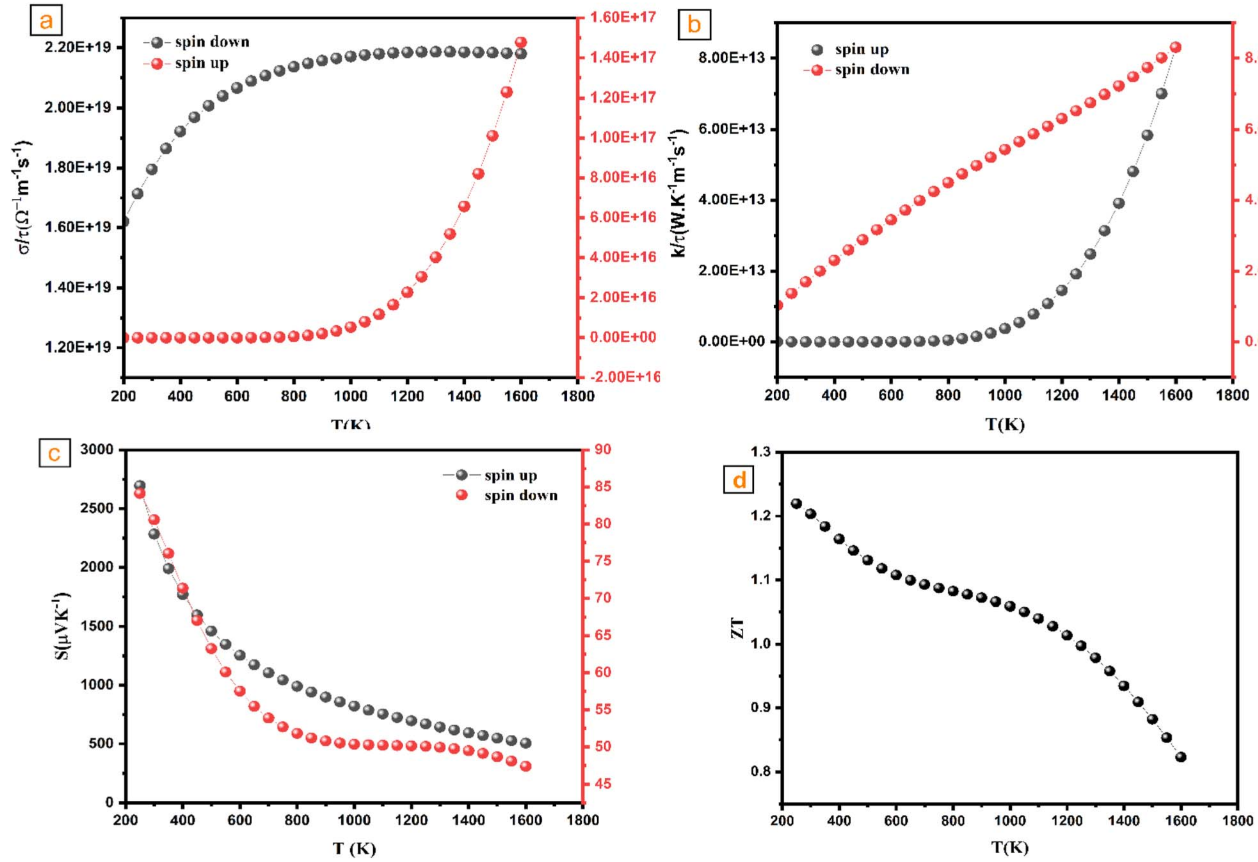

Fig. 10 (a) Variation of electron conductivity, (b) thermal conductivity, (c) total Seebeck coefficient, and (d) *ZT* factor.

In contrast, $La_{0.5}Sm_{0.2}Sr_{0.3}MnO_3$ exhibits a higher figure of merit with *ZT* reaching 1.22, which can be attributed to the optimized electronic structure resulting from Sm and Sr substitution at the La site.[41]

This comparative analysis confirms that $La_{0.5}Sm_{0.2}Sr_{0.3}MnO_3$ exhibits enhanced multifunctional properties, making it a strong candidate for applications in magnetic refrigeration and thermoelectric energy conversion devices.

5 Conclusion

The $La_{0.5}Sm_{0.2}Sr_{0.3}MnO_3$ compound was successfully synthesized using the glycine-nitrate procedure GNP. DFT and MFT theoretical approaches have led to a better understanding of the electronic, magnetic, optical and thermoelectric properties of this material. Electronic structure analysis revealed that $La_{0.5}Sm_{0.2}Sr_{0.3}MnO_3$ exhibits semi-metallic behavior, with strong covalent interactions between Mn, Sm and O ions contributing to its metallic characteristics. The compound also displays notable ferromagnetic behavior, with a second-order magnetic transition from the ferromagnetic to the paramagnetic state at 278 K. In addition, the optical properties indicate potential applications in solar cells and optoelectronic devices, due to the high absorption of the material in the UV-A range. Finally, the thermoelectric analysis demonstrated that $La_{0.5}Sm_{0.2}Sr_{0.3}MnO_3$ is promising for the integration of thermoelectric devices, with a *ZT* value reaching 1.22 at 200 K. These findings highlight the versatility of $La_{0.5}Sm_{0.2}Sr_{0.3}MnO_3$, making it a promising material for applications in electronics, magnetism, optics, and thermoelectricity.

Author contributions

A. Mabrouki: writing, performed DFT calculations. Khouloud Abdouli: writing, methodology, validation. Afrah Bardaoui: conceptualization, methodology, validation. O. Messaoudi: investigation, visualization, writing, original draft preparation. Latifah Alfhaid: writing, conceptualization, methodology, validation. Amjad S. Aljaloud: supervisor, methodology, validation.

Conflicts of interest

The authors declare that they have no known competing financial interests or personal relationships that could have appeared to influence the work reported in this paper.

Data availability

No primary research results, sotware or code have been included and no new data were generated or analysed as part of this review.

Open Access Article. Published on 15 October 2025. Downloaded on 5/10/2026 3:55:54 AM.
This article is licensed under a Creative Commons Attribution-NonCommercial 3.0 Unported Licence.

Acknowledgements

This research has been funded by the Research Deanship of the University of Ha'il-Saudi Arabia through Project Number RG-23 135.

References

1 A. Mabrouki, O. Messaoudi, A. Bardaoui, A. S. Aljaloud, L. Alfhaid and E. Dhahri, Multifunctional properties of a novel $Ba_2MnV_{0.7}Zr_{0.3}O_6$ multiferroic double perovskite, *New J. Chem.*, 2025, **49**, 16295–16306, DOI: **10.1039/D4NJ03929G**.

2 A. Zaafouri, M. Megdiche, S. M. Borchani, O. Messaoudi, A. Mabrouki, L. Alfhaid, *et al.*, AC Conductivity and Dielectric Behavior of a New Double Perovskite PrNaMnMoO6 System, *J. Low Temp. Phys.*, 2023, **210**, 464–483, DOI: **10.1007/s10909-022-02884-9**.

3 O. Messaoudi, A. E. Mabrouki, L. Alfhaid, L. Manai and A. Azhary, Effect of annealing temperature on the photocatalytic activity of La0.8Nd0.1Sr0.1MnO3 manganite for methyl orange degradation and study of its thermoelectric properties using DFT calculations, *J Mater Sci: Mater Electron*, 2023, **34**, 827, DOI: **10.1007/s10854-023-10210-6**.

4 A. Bougoffa, A. Eddin Mabrouki, A. Trabelsi, E. Dhahri and K. Khirouni, Photovoltaic properties of new solar cell based on ideal cubic NaNbO 3 thin films: a combined experimental and density functional theory study, *RSC Adv.*, 2023, **13**, 30092–30100, DOI: **10.1039/D3RA04084D**.

5 A. Mabrouki, A. Bougoffa, A. Trabelsi, E. Dhahri and K. Khirouni, Optical and thermoelectric properties of NaNbO3 thin film deposed by spray pyrolysis: experimental and DFT study, *Eur. Phys. J. Plus*, 2022, **137**, 748, DOI: **10.1140/epjp/s13360-022-02963-6**.

6 A. E. Mabrouki, O. Messaoudi and L. H. Alfhaid, Synthesis and Investigation of Optical, Magnetic, and Thermoelectric Properties of Li0.5Zr0.5Mg0.5Fe1.5O4 Spinel and First-Principles Characterization as an Electrode Material for Li-Ion Batteries, *Cryst. Growth Des.*, 2023, **23**, 6526–6534, DOI: **10.1021/acs.cgd.3c00487**.

7 A. E. Mabrouki, O. Messaoudi, A. Dhahri, A. Azhary, M. Mansouri and L. Alfhaid, Investigation of the Frequency-Dependent Dielectric Properties of the As-Prepared LaNiO3/Co3O4 Nanocomposites, *ACS Omega*, 2025, **10**, 22701–22710, DOI: **10.1021/acsomega.4c11199**.

8 N. Hamdaoui, D. Tlili, Y. Azizian-Kalandaragh, B. Zaidi, S. Zemni, A. A. Akl, *et al.*, Effect of Ni-doping on the structural, magnetic, and electronic properties of La0.2Sr0.8MnO3 perovskite, *J. Mater. Sci.: Mater. Electron.*, 2021, **32**, 26984–26997, DOI: **10.1007/s10854-021-07072-1**.

9 A. Saidi, A. Mabrouki, J. Dhahri, E. Dhahri, K. Khirouni and B. F. O. Costa, Effect of frequency on the classical and relaxor ferroelectric behavior of substituted titanate Ba0.7Er0.16Ca0.05Ti0.91Sn0.09O3, *Phys. Chem. Chem. Phys.*, 2023, **25**, 17999–18010, DOI: **10.1039/D3CP01273E**.

10 A. Saidi, A. Mabrouki, R. Dhahri, E. Dhahri, K. Khirouni and B. F. O. Costa, Electronic, electrical and thermoelectric properties of Ba0.95Ca0.05Ti0.95Y0.05O2.975 compound: Experimental study and DFT-mBJ calculation, *Heliyon*, 2023, **9**, e18780, DOI: **10.1016/j.heliyon.2023.e18780**.

11 A. Jeidd, M. Amghar, A. Mabrouki, A. Benali, A. Trabelsi, E. Dhahri, *et al.*, Study of physical properties of the Li 0.5 MgFe 1.5 O 3.5 ferrite nanoparticles, *RSC Adv.*, 2023, **13**, 12906–12916, DOI: **10.1039/D2RA07970D**.

12 N. N. Loshkareva, S. YuP, E. V. Mostovshchikova, L. V. Nomerovannaya, A. A. Makhnev, S. V. Naumov, *et al.*, The evolution of the optical spectra of LaMnO3 under light n-and p-type doping and the separation of phases, *J. Exp. Theor. Phys.*, 2002, **94**, 350–355, DOI: **10.1134/1.1458485**.

13 T. Zhang, R. Wan, Y. Guo, A. J. Ahmed, Y. Lei and G. Tian, Lanthanum-doped SrTiO3 theoretical thermoelectric properties, *Ionics*, 2022, **28**, 2021–2028, DOI: **10.1007/s11581-021-04410-5**.

14 G. Sclauzero and C. Ederer, Structural and electronic properties of epitaxially strained from density functional theory and dynamical mean-field theory, *Phys. Rev. B:Condens. Matter Mater. Phys.*, 2015, **92**, 235112, DOI: **10.1103/PhysRevB.92.235112**.

15 H. Wadati, J. Mravlje, K. Yoshimatsu, H. Kumigashira, M. Oshima, T. Sugiyama, E. Ikenaga, A. Fujimori, A. Georges, A. Radetinac, K. S. Takahashi, M. Kawasaki and Y. Tokura, Photoemission and DMFT study of electronic correlations in SrMoO3: effects of Hund's rule coupling and possible plasmonic sideband, *Phys. Rev. B:Condens. Matter Mater. Phys.*, 2014, **90**, 205131, DOI: **10.1103/PhysRevB.90.205131**.

16 M. Arejdal, M. Kadiri, A. Abbassi, A. Slassi, A. A. Raiss, L. Bahmad, *et al.*, Magnetic Properties of the DoublePerovskite Ba2CoUO6: *Ab Initio* Method, Mean Field Approximation, and Monte Carlo Study, *J. Supercond. Novel Magn.*, 2016, **29**, 2659–2667, DOI: **10.1007/s10948-016-3598-8**.

17 K. Abdouli, W. Cherif, H. Omrani, M. Mansouri, M. A. Valent, M. P. F. Graça, *et al.*, Structural, magnetic and magnetocaloric properties of La0.5Sm0.2Sr0.3Mn1-xFexO3 compounds with ($0 \leq x \leq 0.15$), *J. Magn. Magn. Mater.*, 2019, **475**, 635–642, DOI: **10.1016/j.jmmm.2018.12.007**.

18 J. Rodriguez-Carvajal. FULLPROF: a program for Rietveld refinement and pattern matching analysis. *Satellite Meeting On Powder Diffraction Of The Xv Congress Of The IUCr*, vol. 127, Toulouse, France; 1990, p. 127.

19 P. Blaha, K. Schwarz, F. Tran, R. Laskowski, G. K. H. Madsen and L. D. Marks, WIEN2k: An APW+lo program for calculating the properties of solids, *J. Chem. Phys.*, 2020, **152**, 074101, DOI: **10.1063/1.5143061**.

20 A. Mabrouki, O. Messaoudi, M. Mansouri, S. Elgharbi and A. Bardaoui, Study of the structural, electronic, magnetic and magnetocaloric properties of La 0.5 Ca 0.5 Mn 0.9 V 0.1 O 3 sample: first-principles calculation (DFT–MFT), *RSC Adv.*, 2021, **11**, 37896–37903, DOI: **10.1039/D1RA07177G**.

© 2025 The Author(s). Published by the Royal Society of Chemistry

Open Access Article. Published on 15 October 2025. Downloaded on 5/10/2026 3:55:54 AM.
This article is licensed under a Creative Commons Attribution-NonCommercial 3.0 Unported Licence.

21 S. Chettri, D. P. Rai, A. Shankar, R. Khenata, M. P. Ghimire, R. K. Thapa and S. Bin Omran, GGA + U and mBJ + U study of the optoelectronic, magnetic and thermoelectric properties of the SmAlO3 compound with spin–orbit coupling, *Int. J. Mod. Phys. B*, 2016, **30**, 1650078, DOI: **10.1142/S0217979216500788**.

22 G. K. H. Madsen, J. Carrete and M. J. Verstraete, BoltzTraP2, a program for interpolating band structures and calculating semi-classical transport coefficients, *Comput. Phys. Commun.*, 2018, **231**, 140–145, DOI: **10.1016/j.cpc.2018.05.010**.

23 J. S. Amaral, S. Das, V. S. Amaral, J. S. Amaral, S. Das and V. S. Amaral, The Mean-Field Theory in the Study of Ferromagnets and the Magnetocaloric Effect, *Thermodynamics - Systems in Equilibrium and Non-equilibrium*, IntechOpen, 2011, DOI: **10.5772/21595**.

24 C. P. Bean, Magnetic Disorder as a First-Order Phase Transformation, *Phys. Rev.*, 1962, **126**, 104–115, DOI: **10.1103/PhysRev.126.104**.

25 I. Dhahri, A. Mabrouki, M. Ellouze, E. Dhahri, S. Labidi, E. K. Hlil, *et al.*, Simulation study by phenomenological and Bean–Rodbell methods of La0.7Sr0.3Mn0.95Fe0.05O3 compound, *Indian J. Phys.*, 2022, **96**, 3509–3515, DOI: **10.1007/s12648-021-02275-y**.

26 A. Mabrouki, T. Mnasri, A. Bougoffa, A. Benali, E. Dhahri and M. A. Valente, Experimental study and DFT calculation of the oxygen deficiency effects on structural, magnetic and optical properties of La0.8□0.2MnO3-δ (δ = 0, 0.1 and 0.2) compounds, *J. Alloys Compd.*, 2021, **860**, 157922, DOI: **10.1016/j.jallcom.2020.157922**.

27 J. Li, The electronic, structural and magnetic properties of La1−1/3Sr1/3MnO3 film with oxygen vacancy: a first principles investigation, *Sci. Rep.*, 2016, **6**, 22422, DOI: **10.1038/srep22422**.

28 R. Asahi, W. Mannstadt and A. J. Freeman, Optical properties and electronic structures of semiconductors with screened-exchange LDA, *Phys. Rev. B:Condens. Matter Mater. Phys.*, 1999, **59**, 7486–7492, DOI: **10.1103/PhysRevB.59.7486**.

29 J. Jiang, Q.-M. Chen and X. Liu, First-principles study on the electronic structure and optical properties of La0.75Sr0.25MnO3-σ materials with oxygen vacancies defects, *Curr. Appl. Phys.*, 2018, **18**, 200–208, DOI: **10.1016/j.cap.2017.12.005**.

30 Y. Gutiérrez, A. S. Brown, F. Moreno and M. Losurdo, Plasmonics beyond noble metals: Exploiting phase and compositional changes for manipulating plasmonic performance, *J. Appl. Phys.*, 2020, **128**, 080901, DOI: **10.1063/5.0020752**.

31 Q. Mahmood, M. Hassan, K. C. Bhamu, M. Yaseen, S. M. Ramay and A. Mahmood, Density functional theory-based study of the magnetic and optical properties of PbMO3 (M = Cr, Fe) using the modified BeckeJohnson mBJ functional, *J. Phys. Chem. Solids*, 2019, **128**, 275–282, DOI: **10.1016/j.jpcs.2017.12.030**.

32 A. Parveen and G. Vaitheeswaran, Exploring Exemplary Optoelectronic and Charge Transport Properties of KCuX(X=Se,Te), *Sci. Rep.*, 2018, **8**, 13071, DOI: **10.1038/s41598-018-31300-0**.

33 M. Amini and A. Gholizadeh, Shape control and associated magnetic and dielectric properties of MFe12O19 (M = Ba, Pb, Sr) hexaferrites, *J. Phys. Chem. Solids*, 2020, **147**, 109660, DOI: **10.1016/j.jpcs.2020.109660**.

34 A. Gholizadeh, A comparative study of physical properties in Fe3O4 nanoparticles prepared by coprecipitation and citrate methods, *J. Am. Ceram. Soc.*, 2017, **100**, 3577–3588, DOI: **10.1111/jace.14896**.

35 J. S. Amaral, M. S. Reis, V. S. Amaral, T. M. Mendonça, J. P. Araújo, M. A. Sá, *et al.*, Magnetocaloric effect in Er- and Eu-substituted ferromagnetic La-Sr manganites, *J. Magn. Magn. Mater.*, 2005, **290–291**, 686–689, DOI: **10.1016/j.jmmm.2004.11.337**.

36 S. Yousuf, T. M. Bhat, S. Singh, Z. Saleem, S. A. Mir, S. A. Khandy, *et al.*, Applicability of semi-classical Boltzmann transport theory in understanding the thermoelectric properties of ZrNiSn and ZrNiPb half-heuslers, *AIP Conf. Proc.*, 2019, **2115**, 030420, DOI: **10.1063/1.5113259**.

37 J. Liu, Q.-Y. Jiang, S.-D. Zhang and H. Zhang, Carrier mobility and relaxation time in BiCuSeO, *Phys. Lett. A*, 2019, **383**, 125990, DOI: **10.1016/j.physleta.2019.125990**.

38 Y. Li, Q.-Y. Hou, X.-H. Wang, H.-J. Kang, X. Yaer and J.-B. Li, First-principles calculations and high thermoelectric performance of La–Nb doped $SrTiO_3$, *J. Mater. Chem. A*, 2019, 7, 236–247, DOI: **10.1039/C8TA10079A**.

39 E. I. Konstantinova, A. A. Markov, M. A. Ryzhkov and I. A. Leonidov, High-temperature thermoelectrical properties of cubic SrMnO3−δ-based manganites, *Solid State Sci.*, 2022, **134**, 107024, DOI: **10.1016/j.solidstatesciences.2022.107024**.

40 A. Kumar, K. Kumari, B. Jayachandran, D. Sivaprahasam and A. D. Thakur, Thermoelectric properties of (1-x) LaCoO3.xLa0.7Sr0.3MnO3 composite, *J. Alloys Compd.*, 2018, **749**, 1092–1097, DOI: **10.1016/j.jallcom.2018.03.347**.

41 J. Park, Y.-N. Wu, W. A. Saidi, B. Chorpening and Y. Duan, First-principles exploration of oxygen vacancy impact on electronic and optical properties of ABO3−δ (A = La, Sr; B = Cr, Mn) perovskites, *Phys. Chem. Chem. Phys.*, 2020, **22**, 27163–27172, DOI: **10.1039/D0CP05445C**.

© 2025 The Author(s). Published by the Royal Society of Chemistry